Poisson-like height distribution of Ag nanoislands on Si(111) 7×7

Yiyao Chen, M. W. Gramlich, S. T. Hayden, and P. F. Miceli*
Department of Physics and Astronomy, University of Missouri, Columbia, Missouri 65211, USA
(Received 12 October 2016; published 20 January 2017)

The height distribution of Ag(111) islands grown on Si(111) 7×7 was studied using *in situ* x-ray reflectivity. This noble metal-on-semiconductor system is of particular interest because the islands exhibit an unusual minimum height that is imposed by the quantum confinement of the conduction electrons. For different coverages and temperatures as well as annealing, it was found that the island heights exhibit a variance that is less than the mean by a constant amount. We argue that this behavior is related to Poisson-like statistics with the imposition of the minimum island height. A modified Poisson height distribution model is presented and shown to provide a good description of the experimentally measured island height distributions. The results, which contribute to a better understanding of the nanoscale growth behavior for an important noble metal, are discussed in terms of mobility that leads to taller islands.

DOI: 10.1103/PhysRevB.95.035419

I. INTRODUCTION

Nanoscale materials are of interest for many reasons, including their utility due to their smallness of size or from improved catalytic properties due to their large surface to volume ratio; but intriguing new physical properties can arise simply because of the nanoscale dimensions [1,2]. These new properties can extend to novel growth phenomena that invoke mechanisms beyond the conventional morphological evolution during film growth [3]. A particularly interesting case concerns nanoscale metallic islands that can exhibit height selection due to the quantum confinement of the conduction electrons, known as quantum size effects (QSE) [4–7]. Oscillatory stability of the island heights on the monolayer scale, the period of which is related to the Fermi wavelength, has been observed during the growth of a number of metals [8–10]. The influence of quantum effects on the growth behavior of metals is important to understand both for fundamental reasons and for new frontiers in nanotechnology where one must know how to control the growth of metals on the nanoscale.

There has been considerable interest to understand the mechanism by which Ag grows on Si(111) 7×7 because it exhibits an intriguing minimum island height that does not occur in the examples given above [11–15]. The growth of Ag(111) islands differs in an important way from systems that exhibit oscillatory island height stability because its Fermi level is in a band gap along [111] so that there is no Fermi wavelength to consider [16,17]. Recently, however, it was noted [18] that the observed minimum island height of Ag(111) can be explained from its thickness-dependent electronic structure [19]. The minimum island height arises from electron quantum confinement effects for very thin layers, albeit not due to a Fermi wavelength so that there is no oscillatory stability.

Ag(111) islands form only after the completion of a Ag wetting layer that occurs during the initial growth on Si(111) 7×7, up to ∼0.4 ML coverage. The Ag wetting layer consists of a discontinuous network of single atomic-layer islands that reside within half-unit-cells of the Si(111) 7×7 reconstructed substrate surface [12,20]. Above ∼0.4 ML coverage, taller Ag(111) islands begin to form [12] so that the Ag/Si system grows in a Stranski-Krastanov (SK) growth mode. The Ag(111) islands were initially believed to exhibit a minimum height of two atomic layers on top of the wetting layer [11–14]. Recent x-ray scattering studies, however, revealed that the islands dissolve the portion of the commensurate wetting layer beneath the islands so that the minimum island height contains *three* atomic layers of FCC Ag having an incommensurate interface directly with the substrate [18]. Above 0.4 ML coverage, it is observed that the atomic scale structure of the discontinuous wetting layer no longer changes or accumulates Ag so that at the 0.4 ML saturation coverage there is a transition to a macroscopic two-phase coexistance of incommensurate FCC Ag(111) islands with the commensurate wetting layer [21].

Although much attention has been given to the minimum island height observed during the growth of Ag(111) on Si, the overall island height distribution has not been carefully considered in the context of taller island heights, which are also observed. For example, the minimum height of three layers is found at a very low coverage just above saturation while a taller average island height emerges with increasing coverage [21]. The island height distribution also depends on temperature: the average island height and the width of the height distribution are found to increase with increasing temperature, which is due to the increased mobility at higher temperature [18]. The height distribution of the islands has neither been considered experimentally nor theoretically in a quantitative manner.

In this paper, we experimentally investigate the evolution of the island height distribution with coverage, temperature, and annealing. For all cases studied, it is found that the variance of the island height distribution follows the mean height, except for an "offset" that reflects the three-layer minimum height. Although this behavior suggests a Poisson-like distribution, it is not strictly a Poisson distribution and we present a modified Poisson model that successfully explains the experimentally observed distribution of island heights. By comparing the model to the data it can be deduced that the kinetic barrier for forming the first three atomic layers is lower than the barrier for forming taller islands so that mobility limits the formation of taller islands. These results provide a much clearer picture of the energetic and kinetic considerations

*micelip@missouri.edu

needed for understanding the growth of Ag islands on Si(111) 7×7.

II. EXPERIMENTAL

X-ray scattering experiments were performed *in situ* in ultrahigh vacuum using the surface scattering chamber (base pressure of 1×10^{-10} Torr) on a PSI diffractometer located at the 6IDC beam line at the Advanced Photon Source. The photon energy was 16.2 keV and the specular reflectivity data were collected in the horizontal scattering plane. The momentum transfer of the specular reflectivity is described in hexagonal coordinates $(0,0,L)_H$, $Q = \frac{2\pi L}{c_H}$, where $c_H = 9.407$ Å, and $[0,0,3]_H = [1,1,1]$ is along the surface normal direction.

Ag was deposited on a clean Si(111) 7×7 surface using a thermal evaporator with a deposition rate of $\sim 1.1 \pm 0.1$ ML/min, where 1 ML is one monolayer of Ag(111)(1 ML $= 1.38\times10^{15}$ atoms/cm^2). The preparation of the Si(111) 7×7 surface, calibration of the Ag deposition rate, and other experimental conditions are described in Ref. [21]. Three series of data were collected in this study. Two series of measurements were performed at a fixed coverage, 0.9 ML and 1.8 ML, for different deposition temperatures. One sample was prepared with a coverage of 0.9 ML deposited at 150 K and then subsequently measured at sequentially higher annealing temperatures.

III. RESULTS

X-ray specular reflectivity was used to study the island height distribution of Ag grown on Si(111) 7×7 for different coverages, deposition temperatures, and annealing temperatures. The results are shown in Fig. 1 for the three series of data. Qualitatively, the reflectivity from N atomic layers of Ag appears as an optical N-slit interference where the Ag Bragg peaks appear as the principle maxima, located at $L = 3.98$ and 7.96, along with $N-2$ interference fringes appearing in between the principle maxima. The width of the Bragg peaks is inversely proportional to N. From Fig. 1 it can be seen that the minimum height is three layers, corresponding to one interference fringe, whereas the average island height increases with increasing coverage or temperature. It is noted that measurements performed just slightly above the wetting layer saturation coverage show the predominance of three-layer islands, which is therefore the minimum island height [21].

The island height distribution p_j, which is defined as the fraction of the surface covered by islands having height j, was determined quantitatively from a fit to the specular reflectivity data using the model presented by Chen *et al.* [21]. The majority of the surface is covered by the wetting layer, with a surface fraction given by p_{wet}, so that conserving the total surface yields $p_{\text{wet}} + \sum_{j=1} p_j = 1$. To analyze the population of the islands, we consider a normalized island height distribution p'_j, which we will refer to as the *island population*, that describes the fraction of the islands having height j. It is given by $p'_j = \frac{p_j}{\sum_{j=2} p_j}$ with $\sum_{j=2} p'_j = 1$, where we have used the fact that omitting p_1 in the normalization has a negligible effect. Although the omission of p_1 was necessary because the commensurate wetting layer and one-layer-thick ($j = 1$) incommensurate FCC Ag islands are not easily distinguished by specular reflectivity, Chen *et al.* [21] demonstrated that p_1 is very small by using complementary crystal truncation rod analysis so that omitting p_1 in the normalization is insignificant. The mean island height of the island population

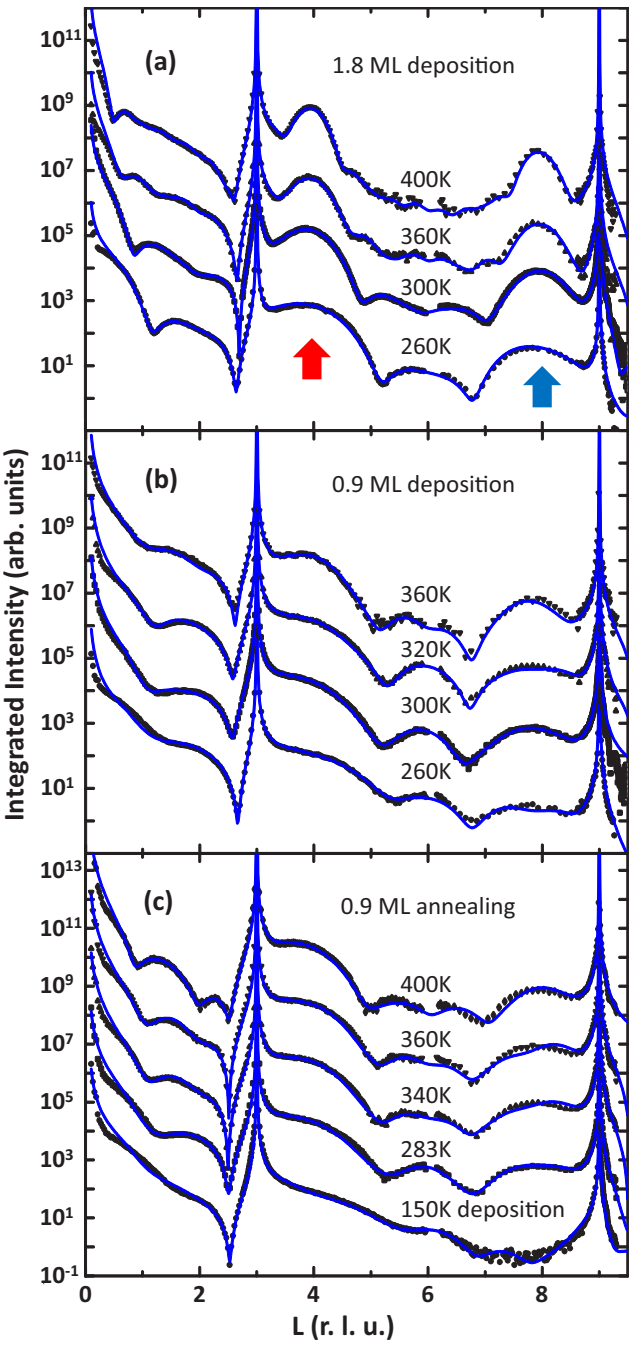

FIG. 1. Specular reflectivity measurements performed for different growth conditions. The data have been offset vertically from each other to provide clarity. (a) 1.8 ML of Ag deposited at the given temperatures; arrows indicate the Ag(111) (red) and Ag(222) (blue) Bragg positions. (b) 0.9 ML of Ag deposited at the given temperatures; (c) 0.9 ML of Ag deposited at 150 K and annealed to the given temperatures. The solid curves are the best fit to a model [21] that allows the determination of the island height distribution.

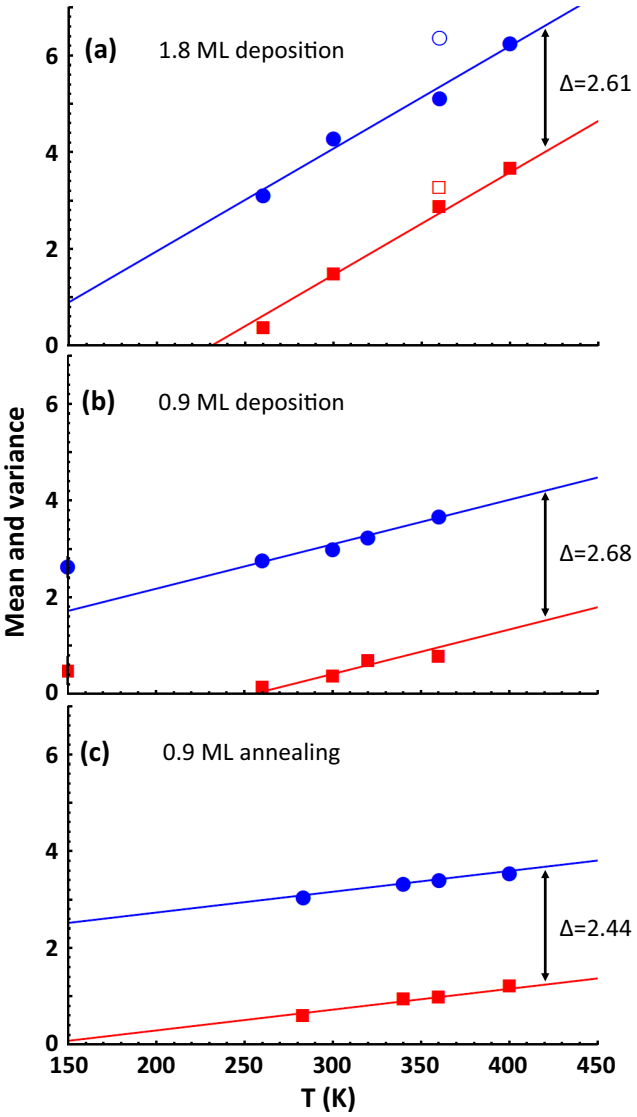

FIG. 2. The mean island height (circles) $\bar{n}$ and the height variance (squares) s^2 of the island population that was determined from the x-ray specular reflectivity data in Fig. 1. (a) 1.8 ML Ag deposited at different temperatures. One measurement for 2.7 ML deposited at 360 K is also plotted with open symbols (its reflectivity data are not shown in Fig. 1). It was not used in the determination of the line. (b) 0.9 ML Ag deposited at different temperatures and (c) annealing at different temperatures for 0.9 ML Ag deposited at 150 K. In each of (a), (b), and (c) one line was obtained by fitting $\bar{n}$, and the other line through the variance data has the same slope with the line shifted downward by Δ.

is given as $\bar{n} = \sum j p'_j$ and the height variance of the island population is given as $s^2 = \sum j^2 p'_j - \bar{n}^2$.

Figure 2 shows the mean island height $\bar{n}$ and the height variance s^2 of the island populations that were determined from the data of Fig. 1. There are a number of important features to notice in this result. The mean height is observed to increase with both increasing temperature and coverage. It is striking that the variance of the island population exactly tracks the mean with a constant difference: $s^2 = \bar{n} - \Delta$, where Δ is a number that is slightly less than three. To emphasize this point

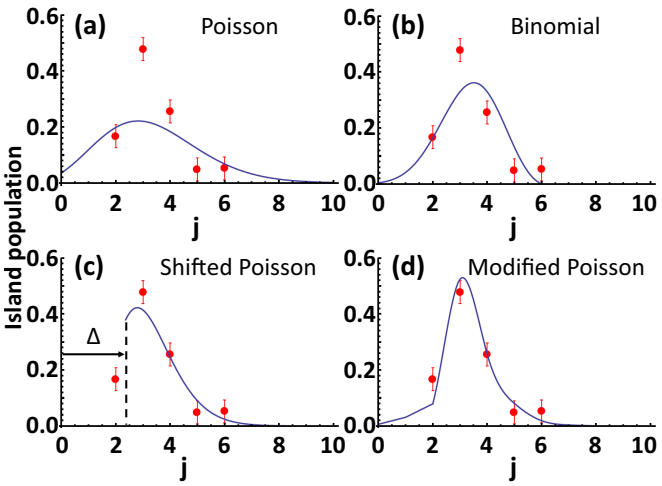

FIG. 3. The island population is plotted versus j for different island population models P_j (solid curve) and compared with the experimental data p'_j (circles) that was obtained from Fig. 1(c) for 0.9 ML Ag annealed to 340 K. The experimental values of $\bar{n} = 3.33$ and $s^2 = 0.97$ are used to calculate the model curves. (a) Poisson distribution; (b) binomial distribution; (c) Poisson distribution shifted by Δ; (d) modified Poisson distribution, as discussed in the text. Factorials in the distributions calculated in (a), (b), and (c) are replaced with the Gamma function, $j! = \Gamma(j+1)$, to generate continuous curves, whereas the modified Poisson distribution in (d) is calculated numerically at integer values and the plotted curve uses an interpolation between discrete points.

in Fig. 2, the line through the variance has the same slope as the line through the mean. One sample was measured for 2.7 ML coverage, shown in Fig. 2(a), and it also follows the same trend (its reflectivity is not given in Fig. 1). A consequence of this relationship between mean and variance is that as the mean approaches three layers, the variance approaches zero and the island height distribution becomes very narrow. In fact, it can be seen in Fig. 2(b) that when the island height approaches three, neither the mean nor the variance continue to decrease between 260 K and 150 K.

In order to interpret the experimental results, we examine several model distributions P_j and compare them with the experimentally determined island population p'_j in Fig. 3. The linear relationship of the experimental mean and variance is suggestive of Poisson statistics where the mean is equal to the variance. Using the experimentally observed mean $\bar{n}$, the Poisson distribution is given as

$$P_j = \frac{\bar{n}^j e^{-\bar{n}}}{j!}. \quad (1)$$

It can be seen from Fig. 3(a) that the Poisson distribution compares quite poorly with the experimental data: Although the mean values agree, the Poisson distribution is far too broad compared to the data because it neglects the narrowing of the variance by an amount Δ.

It is apparent that having only a single parameter $\bar{n}$ in the Poisson distribution is insufficient to capture both the mean and the variance of the data. Therefore, we also tested the binomial distribution, which has the mean and variance as two

independent parameters, and it is given as

$$P_j = \frac{M!}{j!(M-j)!} p^j (1-p)^{M-j}, \tag{2}$$

where M is an integer and $0 \leqslant p \leqslant 1$. Although the mean is given as $\bar{n} = Mp$ and the variance is $s^2 = Mp(1-p)$, one must be cautious in calculating M and p from the experimental mean and variance if M is to be an integer. This constraint was accomplished by first determining $M = \frac{\bar{n}}{1-s^2/\bar{n}}$ rounded up to the nearest integer, and then p was subsequently calculated as $p = \frac{\bar{n}}{M}$. As shown in Fig. 3(b), using the experimental values for both the mean and the variance allows the binomial distribution to describe the data better than the Poisson distribution; however, the shape of the binomial distribution is not correct because the width of the distribution is too broad and its height is too low.

Because of the linear relationship between the mean and the variance that is exhibited in the experimental data of Fig. 2, it is instructive to take a closer look at the Poisson distribution. Utilizing the experimentally observed variance in the distribution, rather than the mean, and then shifting the distribution by $\Delta = \bar{n} - s^2$ to obtain the observed mean gives

$$P_j = \frac{(s^2)^{j-\Delta} e^{-s^2}}{\Gamma(j-\Delta+1)}. \tag{3}$$

As shown in Fig. 3(c), the shifted Poisson distribution matches the data quite well in its region of validity, $j \geqslant \Delta$, because using s^2 rather than $\bar{n}$ leads to a narrowing of the distribution. The model, however, does not describe $j < \Delta$.

We interpret these results to suggest that Poisson-like island height fluctuations occur except that the fluctuations encounter the three-layer minimum island height, which provides a lower bound to the fluctuations. Indeed, the variance is reduced from the mean by an amount Δ, which is slightly less than three. With this insight, below we explore a model that modifies the conventional Poisson distribution by favoring the growth of the first three layers. As can be seen from Fig. 3(d), this modified Poisson distribution model captures the essential features of the experimental data: It describes the Poisson-like tails at high j, and it attenuates the distribution at low j.

In contrast to the conventional derivation of the Poisson distribution [22], which assumes all events occur with the same probability, we consider that the probability per time to increment the height of an island by one atomic layer λ_j depends on the island height j. After a time increment of dt, the resulting probability to have the surface covered by islands of height j is given as

$$P_j(t+dt) = P_{j-1}(t)\lambda_{j-1}dt + P_j(t)(1-\lambda_j dt), \tag{4}$$

where the first term is the probability to add one more layer on top of islands having height $j-1$, and the second term is the probability that a layer is not added to islands having height j. Solving the resulting differential equation, $\frac{dP_j(t)}{dt} + \lambda_j P_j(t) = \lambda_{j-1} P_{j-1}(t)$, leads to a recursive solution,

$$P_j(t) = e^{-\lambda_j t} \int_0^t \lambda_{j-1} P_{j-1}(t') e^{\lambda_j t'} dt'. \tag{5}$$

Given the boundary condition, $P_j = 0$ for $j < 0$, and the initial condition that the P_j are normalized at $t = 0$, it can be shown that the normalization holds for all time, $\sum_{j=0} P_j(t) = 1$, as well as $P_0(t) = e^{-\lambda_0 t}$. Further, it can be shown that the mean is given by

$$\bar{n}(t) = \sum_{j=0}^{\infty} \lambda_j \int_0^t P_j(t')dt' = \sum_{j=0}^{\infty} j P_j(t), \tag{6}$$

and the variance is

$$s^2(t) = \bar{n}(t) + 2\sum_{j=0}^{\infty} j\lambda_j \int_0^t P_j(t')dt' - \bar{n}^2(t)$$

$$= \sum_{j=0}^{\infty} j^2 P_j(t) - \bar{n}^2(t). \tag{7}$$

The limit where all $\lambda_j = \lambda$ are the same leads to the conventional Poisson distribution whereby the mean and variance are equal, $\lambda t = \bar{n} = s^2$. The Poisson distribution has been previously used in "hit and stick" models of epitaxial growth where atoms cannot leave the terrace upon which they were deposited [23]. It has been shown that Poisson statistics apply to the homoepitaxial growth of Ag(111) where there is a large barrier to diffusion over crystalline step edges so that deposited atoms cannot leave their terraces [24,25]. In the present modified Poisson distribution model, however, lateral mobility is intrinsic to the model as the deposition increment $\lambda_j dt$ includes atoms that are both directly deposited onto an island of height j as well as those that migrate to or from there. Indeed, the contribution from deposition is absent in the case of annealing.

Since the modified Poisson distribution contains many parameters, we seek the minimal model with the least number of parameters that can explain the experimental results. We found that two parameters are sufficient to explain the data where we use $\lambda_j = \lambda_0$ for $j \leqslant J$ and $\lambda_j = \lambda$ for $j > J$ with J

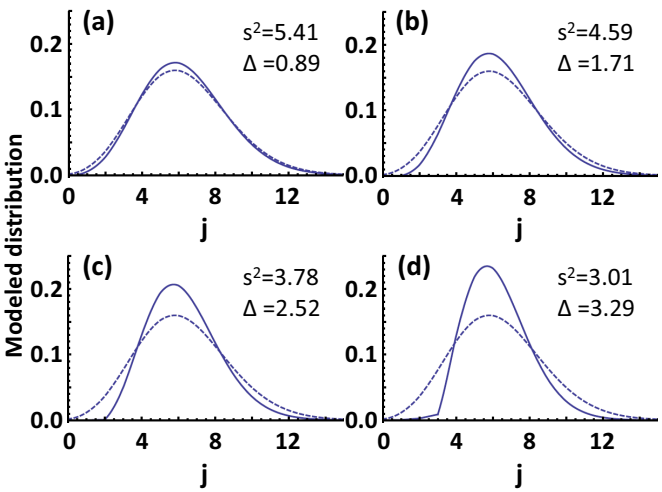

FIG. 4. The modified Poisson distribution (solid curve) with two parameters is calculated for different J using a mean of 6.30 and $\lambda_0 = 2.5\lambda$: (a) $J = 0$, (b) $J = 1$, (c) $J = 2$, and (d) $J = 3$. For comparison, the Poisson distribution (dashed curve) is also shown for $\bar{n} = s^2 = 6.30$. It can be seen that P_j is very small for $j \leqslant J$ and the variance is reduced from the mean by Δ.

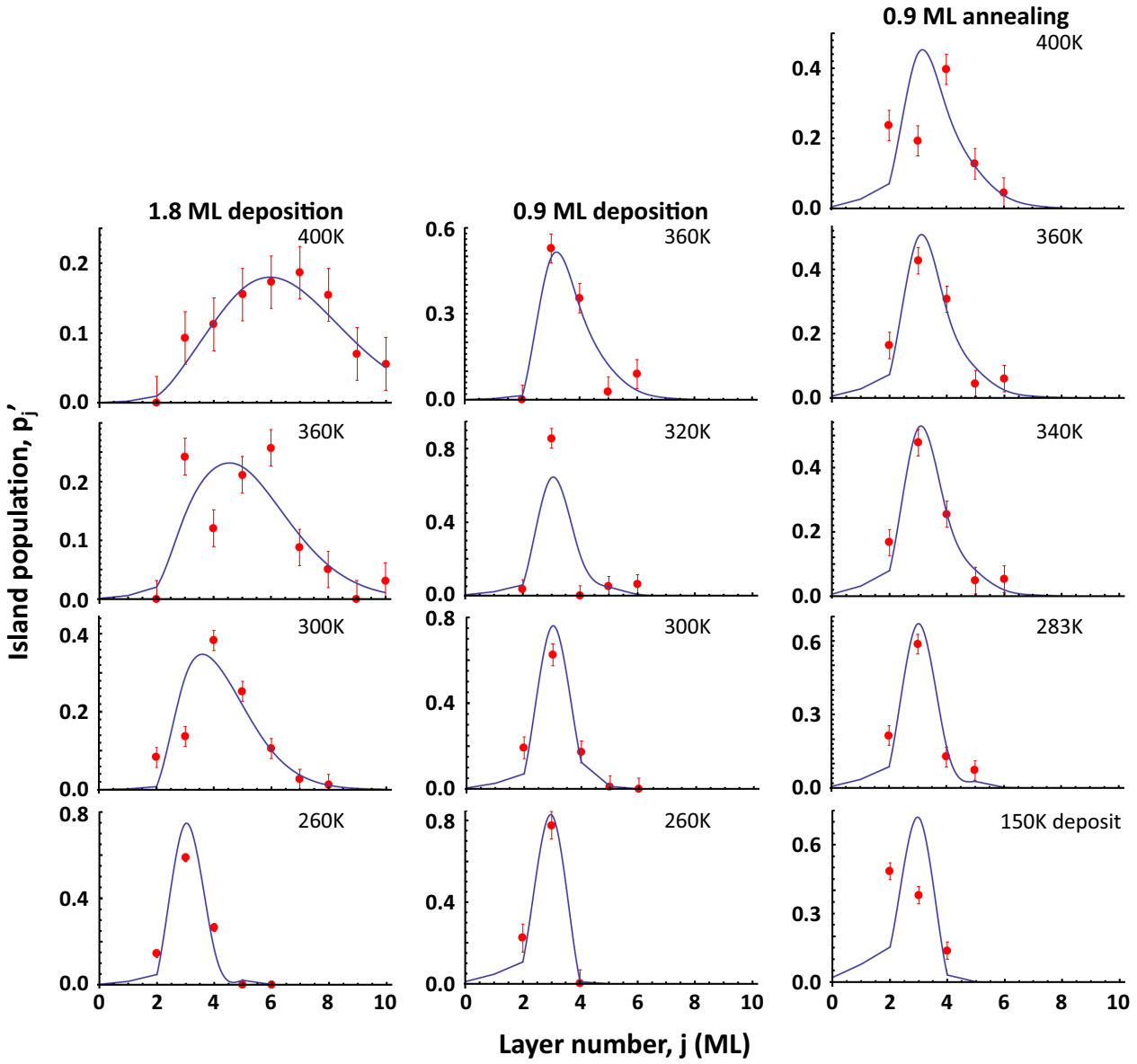

FIG. 5. The modified Poisson distribution model P_j (solid curve) is compared with the experimental island population p'_j (points) that was determined from the x-ray specular reflectivity measurements. The model distribution was calculated using the experimentally determined mean $\bar{n}$ and variance s^2. A cubic spline curve is used to connect discretely calculated points of the model distribution, except at small j, as described in the text.

being an integer. For the three-layer minimum height observed experimentally for Ag(111), we use $J = 2$. It was found that $\lambda_0 < \lambda$ does not lead to an acceptable shape of the distribution as compared with the data. Using more than two values for λ_j can lead to parameter degeneracies for the same distribution P_j, and this problem did not occur using two parameters.

The effect of changing J is explored in Fig. 4 for $\bar{n} = 6.3$ and fixed $\lambda_0/\lambda = 2.5$. As can be seen, P_j is suppressed for $j \leqslant J$. This effect leads to the variance decreasing from $\bar{n}$ with increasing J because the model imposes a lower bound to the height fluctuations. In the two parameter model, the mean and variance can be simplified from Eqs. (6) and (7):

$$\bar{n}(t) = \lambda t + (\lambda_0 - \lambda) \sum_{j=0}^{J} \int_0^t P_j(t')dt', \tag{8}$$

and,

$$s^2(t) = \bar{n}(t) + 2(\lambda_0 - \lambda) \sum_{j=0}^{J} \int_0^t j\, P_j(t')dt' + 2\lambda \int_0^t \bar{n}(t')dt' - \bar{n}^2(t), \tag{9}$$

where $P_j(t)$ only enters for $j \leqslant J$ so that it is taken from the Poisson distribution in Eq. (1) with its mean replaced by $\lambda_0 t$.

Our calculations of P_j used two parameters, λt and λ_0/λ, and a given J. The integrations in Eq. (5) were first performed symbolically using *Mathematica* [26] to obtain $P_j(t)$ in analytical form. Numeric values of the two parameters were then assigned and the distribution was calculated. The P_j were renormalized by $\sum_{j=2}^{\infty} P_j$ in order to compare with the

TABLE I. Summary of the results. The mean and variance, $\bar{n}$ and s^2, were calculated from the experimental island population, and these values were used to determine λt and λ_0/λ according to the modified Poisson distribution model, as discussed in the text. The model distributions shown in Fig. 5 were calculated from these values.

	Coverage	Temperature	$\bar{n}$	s^2	λt	λ_0/λ
deposition	2.7 ML	360 K	6.39	3.30	5.13	2.0
	1.8 ML	400 K	6.27	3.70	5.62	1.45
	1.8 ML	360 K	5.13	2.90	3.76	1.9
	1.8 ML	300 K	4.29	1.51	2.01	4.2
	1.8 ML	260 K	3.12	0.40	0.42	14
	0.9 ML	360 K	3.68	0.81	1.15	6.6
	0.9 ML	320 K	3.25	0.71	0.79	6.8
	0.9 ML	300 K	3.00	0.40	0.33	16
	0.9 ML	260 K	2.78	0.17	0.056	80
	0.9 ML	150 K	2.65	0.50	0.098	40
annealing	0.9 ML	400 K	3.55	1.25	1.51	3.5
	0.9 ML	360 K	3.41	1.01	1.22	4.3
	0.9 ML	340 K	3.34	0.97	1.11	4.6
	0.9 ML	283 K	3.06	0.62	0.55	9.0

p'_j of the experimental island population data, although this correction was negligible because the P_j are small for $j < 2$. At the two highest temperatures for 1.8 ML, the experimental distribution was not determined to sufficiently large j so that in those cases both the experimental distribution and the model were normalized by the sum of j points in the distribution that exist in the experimental data. To generate the model curves in Figs. 3(d), 4, and 5, a cubic spline was used to make a continuous plot of the discrete P_j distribution. In the low-j regions where the distribution drops quickly to zero, the cubic spline creates artifactual oscillations so that a linear interpolation was used in those regions.

The two-parameter modified Poisson distribution model, with $J = 2$, is compared with the experimentally measured distributions p'_j in Fig. 5. Rather than fitting the model distribution to the experimental distribution, we performed a more stringent test by calculating the model distribution from the experimentally determined mean and variance: Using Eqs. (8) and (9) with the experimental $\bar{n}$ and s^2, we numerically solved for λt and λ_0/λ which were then used to calculate the model distribution.

As can be seen from Fig. 5, the agreement between the modified Poisson distribution and the experimental data is quite good. The modified Poisson model is particularly necessary for cases of low $\bar{n}$ where the distribution becomes very narrow and the conventional Poisson or binomial distributions will not match the data, as was demonstrated in Fig. 3. The results are summarized in Table I.

IV. DISCUSSION

The experimentally observed island height distribution exhibits a number of intriguing properties that are associated with the underlying physics of the island growth. Because the variance is equal to the mean minus a constant Δ, which is a number that is slightly less than the three-layer minimum height, the variance becomes very small as the mean island height approaches Δ. This property of the variance implies that the three-layer minimum island height is a strong constraint such that fluctuations cannot easily produce island heights less than three layers. The effect is strikingly manifested in Fig. 2(b) where *both* the mean and the variance saturate to their minimum values for the 0.9 ML data between 150 K and 260 K. Therefore, these observations suggest that a relatively large electronic energy barrier prohibits the formation of islands having less than three layers, but the formation of taller islands is limited by mobility. Indeed, raising the temperature leads to a taller mean island height with the variance reflecting the fact that fluctuations are bounded from below at the three-layer minimum.

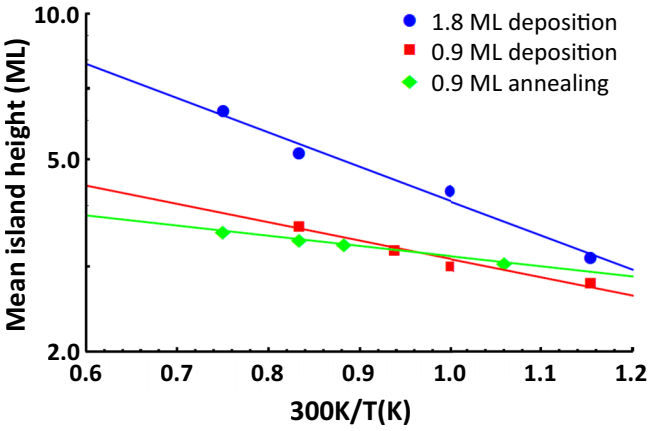

FIG. 6. The experimentally measured mean island height $\bar{n}$ versus inverse temperature for different coverages and for annealing. An Arrhenius behavior is observed and the solid lines were obtained from a fit to the data, as described in the text.

The important role of thermal mobility is highlighted by the observation of an Arrhenius behavior for the mean island heights, as shown in Fig. 6. An activation barrier E_b was determined for each of our three sets of data by assuming that the mean island height is proportional to $e^{-\frac{E_b}{k_B T}}$. For 0.9 ML and 1.8 ML deposition, E_b was found to be 21.5 meV and 42.2 meV, respectively, and 12.5 meV for 0.9 ML annealing, with each having an uncertainty of ± 5 meV. The activation barrier is largest for the highest coverage where the additional quantity of material is more difficult to move. For 0.9 ML coverage, deposition and annealing yield activation energies that differ by slightly less than two error bars, although, the annealing data clearly have the lower activation barrier as is apparent from Fig. 6. However, one must be careful in interpreting the activation barrier when comparing annealing with deposition because the two cases do not have the same initial configuration. Low temperature deposition necessarily leads to a higher island density and a correspondingly smaller lateral island size, which establishes a different initial morphology for the annealing measurements. That morphology can inhibit island height changes during annealing over a *limited* temperature range, and it would *effectively* lead to a smaller apparent activation barrier. This interpretation is consistent with early work that reported smoother surfaces using a two-step deposition process where

low-temperature deposition is followed by higher-temperature annealing [11].

Our experimental results, therefore, indicate that energetic as well as kinetic considerations are both necessary for understanding the full range of the observed growth morphology of Ag islands on Si(111) 7×7, which we now describe. Ag/Si(111) 7×7 follows a SK growth mode where the commensurate Ag wetting layer completely covers the surface before the incommensurate FCC islands can form, which happens because the wetting layer has a lower energy per area than the islands. Amongst different island heights compared at the same coverage, however, taller islands have a lower energy per area than shorter islands due to the interfacial surface tension. Therefore, in equilibrium SK growth would lead to very tall islands coexisting with the wetting layer. In practice, however, limited adatom mobility constrains the vertical growth of islands so that raising the substrate temperature or increasing the coverage will lead to a taller average island height, as is observed experimentally in Fig. 6. For Ag/Si(111) 7×7 this kinetic limitation is very strong as the island heights in the studied temperature range are typically less than ten atomic layers. However, there is an additional consideration for Ag/Si(111) 7×7 that is indicated by experiments: It is energetically expensive to create islands having heights less than three atomic layers. This fact is clearly revealed in the present work where the measured height distributions are observed to decay below three atomic layers. The energetically imposed three-layer minimum height is quite robust as it can lead to a strikingly narrow height distribution having a very small variance when the temperature or coverage is reduced, as observed in Fig. 2. However, even the three-layer minimum height condition will break down at sufficiently low temperature when the mobility is severely limited. This effect can be seen in Fig. 5 at 150 K, which is the lowest growth temperature studied, where there is a significant population of two-layer islands because of the kinetic limitation at this temperature. Therefore, the temperature-dependent height distribution of the Ag islands can be understood in the context of SK growth and the unique energy landscape of Ag/Si(111) 7×7, which determines the mobility barriers.

In addition to the good agreement between the modified Poisson distribution model and the experimental data shown in Fig. 5, the model relates well to the physical interpretation of the growth process, described above. With $\lambda_0 > \lambda$ and $J = 2$, the three-layer islands will form more easily than the taller islands, consistent with the above discussion. However, we also find that the slower kinetics for forming the taller islands is evident from our analysis performed in another important way: We have investigated the temperature dependence of λ_0/λ from Table I and find that the activation barrier to form the three-layer islands is indeed lower than the barrier for forming the taller islands.

In conclusion, the height distribution of Ag(111) islands grown on Si(111) 7×7 have a mean and variance that exhibit a Poisson-like behavior. The minimum three-layer height of Ag(111) islands imposes a significant narrowing of the island height distribution at low coverage whereas the distribution approaches the Poisson limit at higher coverage. Quantum confinement of the conduction electrons determines the minimum Ag(111) island height whereas the formation of the taller islands is limited by mobility. The experimentally measured island height distributions are well described by a modified Poisson model that distinguishes the rate of forming the minimum-height islands from that of the taller islands. Because of its simplicity as a noble metal, these results for Ag on Si(111) 7×7 provide a useful model system for understanding the physical mechanisms that operate during the growth of nanoscale metals on insulating substrates.

ACKNOWLEDGMENTS

Support from the National Science Foundation under Grants No. DMR-0706278 and No. DGE-1069091 is gratefully acknowledged. The Advanced Photon Source at Argonne National Laboratory and the beam line at Sector 6 are supported by the U.S. DOE under Contract No. W-31-109-Eng-38.

[1] K. J. Klabunde and R. M. Richards (eds.), *Nanoscale Materials in Chemistry*, 2nd ed. (John Wiley & Sons, Inc., Hoboken, 2009).
[2] L. M. Liz-Marzán and P. V. Kamat, *Nanoscale Materials* (Kluwer Academic Publisher, Norwell, MA, 2004).
[3] J. W. Evans, P. A. Thiel, and M. C. Bartelt, Surf. Sci. Rep. **61**, 1 (2006).
[4] F. K. Schulte, Surf. Sci. **55**, 427 (1976).
[5] P. J. Feibelman, Phys. Rev. B **27**, 1991 (1983).
[6] M. Ozer, C.-Z. Wang, Z. Zhang, and H. Weitering, J. Low Temp. Phys. **157**, 221 (2009).
[7] W. B. Su, C. S. Chang, and T. T. Tien, J. Phys. D **43**, 013001 (2010).
[8] M. Hupalo, S. Kremmer, V. Yeh, L. Berbil-Bautista, E. Abram, and M. C. Tringides, Surf. Sci. **493**, 526 (2001).
[9] D.-A. Luh, T. Miller, J. J. Paggel, M. Y. Chou, and T.-C. Chiang, Science **292**, 1131 (2001).
[10] A. Gray, Y. Liu, H. Hong, and T. C. Chiang, Phys. Rev. B **87**, 195415 (2013).
[11] L. Gavioli, K. R. Kimberlin, M. C. Tringides, J. F. Wendelken, and Z. Zhang, Phys. Rev. Lett. **82**, 129 (1999).
[12] P. Sobotik, I. Ost'adal, J. Myslivecek, T. Jarolimek, and F. Lavicky, Surf. Sci. **482–485**, 797 (2001).
[13] W. B. Su, H. Y. Lin, Y. P. Chiu, H. T. Shih, T. Y. Fu, Y. W. Chen, C. S. Chang, and T. T. Tsong, Phys. Rev. B **71**, 073304 (2005).
[14] B. Unal, A. Belianinov, P. A. Thiel, and M. C. Tringides, Phys. Rev. B **81**, 085411 (2010).
[15] D. K. Goswami, K. Bhattacharjee, B. Satpati, S. Roy, P. V. Satyam, and B. N. Dev, Surf. Sci. **601**, 603 (2007). Although these authors report oscillatory growth, it has not been observed in other studies reported in the literature.
[16] G. Neuhold and K. Horn, Phys. Rev. Lett. **78**, 1327 (1997).
[17] L. Basile, H. Hong, P. Czoschke, and T.-C. Chiang, Appl. Phys. Lett. **84**, 4995 (2004).
[18] Y. Chen, M. W. Gramlich, S. T. Hayden, and P. F. Miceli, Phys. Rev. Lett. **114**, 035501 (2015).
[19] Y. Han and D.-J. Liu, Phys. Rev. B **80**, 155404 (2009).

[20] I. Ost'adal, P. Sobotik, J. Myslivecek, and T. Jarolimek, Czech. J. Phys. **49**, 1613 (1999).
[21] Y. Chen, M. W. Gramlich, S. T. Hayden, and P. F. Miceli, Phys. Rev. B **94**, 045437 (2016).
[22] A. C. Melissinos, *Experiments In Modern Physics* (Academic Press, New York, 1966).
[23] J. W. Evans, Phys. Rev. B **39**, 5655 (1989).
[24] W. C. Elliott, P. F. Miceli, T. Tse, and P. W. Stephens, Phys. Rev. B **54**, 17938 (1996).
[25] W. C. Elliott, P. F. Miceli, T. Tse, and P. W. Stephens, NATO ASI Ser., Ser. B **360**, 209 (1997).
[26] Wolfram Research, Inc., Mathematica 10.1 (2015).